Porous Fe$_2$O$_3$ nanotubes with α-γ phase junction for enhanced charge separation and photocatalytic property produced by molecular layer deposition

Chaoqiu Chen[a,*], Feifei Duan[a], Shichao Zhao[a], Weike Wang[a,c], Fan Yang[c], Wiwat Nuansing[c], Baiyan Zhang[a,b], Yong Qin[a,b,*], Mato Knez[c,d]

[a] *State Key Laboratory of Coal Conversion, Institute of Coal Chemistry, Chinese Academy of Sciences, Taiyuan, 030001, PR China*
[b] *Center of Materials Science and Optoelectronics Engineering, University of Chinese Academy of Sciences, Beijing, 100049, PR China*
[c] *CIC nanoGUNE Consolider, Donostia, San Sebastian, 20018, Spain*
[d] *IKERBASQUE, Basque Foundation for Science, 48011, Bilbao, Spain*

ABSTRACT

Constructing nanotubular morphologies and heterojunctions are two effective strategies to enhance the charge separation and transport of α-Fe$_2$O$_3$ for improved photocatalytic performance, while the fabrication of porous α-Fe$_2$O$_3$ nanotubes with precisely tailored wall thickness, pore structure, crystallinity, and junctions still remains a big challenge. Herein, two novel molecular layer deposition (MLD) procedures are designed to prepare porous Fe$_2$O$_3$ nanotubes with tunable pore structure and phase junction. The organic fractions of the obtained Fe-hybrid MLD films not only act as soft templates to generate nanopores in nanotube walls but also play a key role in the formation of phase-junction. The porous structure and phase-junction significantly improve the mass diffusion and charge separation efficiency of Fe$_2$O$_3$ nanotubes, leading to a drastically increased photocatalytic activity for photo-Fenton reaction. Especially, the porous α-γ Fe$_2$O$_3$ nanotubes produced by two-step AB MLD from iron tert-butoxide and ethylene glycol exhibit the highest photocatalytic activity, which is more than a 6.5-fold and 20-fold improvement compared with the nonporous pure α-Fe$_2$O$_3$ nanotubes and commercial α-Fe$_2$O$_3$ nanoparticles, respectively. The MLD method provides a new bottom-up approach to develop efficient Fe$_2$O$_3$ based heterostructure porous photocatalysts for waste-water cleaning and water splitting.

1. Introduction

Hematite (α-Fe$_2$O$_3$) has been demonstrated great potentials in hydrogen generation, solar energy utilization, and environmental remediation, owing to its low cost, excellent stability, and suitable bandgap (2.0–2.2 eV) to absorb a large fraction of the solar spectrum [1–5]. Frustratingly, despite the great progresses that have been achieved over the past few years, the energy conversion efficiency of α-Fe$_2$O$_3$ is still far below what is anticipated. One key issue related to this problem is the sluggish kinetics of charge carrier transfer and the resulting high charge recombination rate upon photo-excitation, due to several critical drawbacks of α-Fe$_2$O$_3$ including short hole diffusion distance (2–4 nm), poor electron-hole pair lifetime (< 10 ps), and poor carrier mobility, which mean that only holes generated in the proximity of catalyst/electrolyte interface could be utilized, and the rest of them are lost through recombination with photo-generated electrons [2,3].

To promote the charge separation in space, several strategies, including nanostructuring, doping, surface treatment, cocatalyst loading or heterojunction, have been proposed [2,5–10].

From the intrinsic views of charge separation process, its efficiency mainly depends on two aspect: migration distance and migration rate of charge carriers. The shorter the migration distance is and the faster the charge carriers migrate, the higher charge separation efficiency becomes. In this regard, minimizing the transfer distance of carriers to the α-Fe$_2$O$_3$ surface is needed for facilitating charge separation and retarding charge recombination. However, α-Fe$_2$O$_3$ is an indirect band gap semiconductor, and hence a relatively thick layer (up to 500–600 nm) of α-Fe$_2$O$_3$ is required to sufficiently absorb sunlight [11,12]. To address these issues, various nanostructured α-Fe$_2$O$_3$ materials including nanopillars [13], nanodentrites [5], hierarchical hollow spheres [14], and nanotubes [10,15], have been fabricated to shorten the distance that holes have to transfer and simultaneously

effectively absorb sunlight via light-trapping. Among them, tubular one-dimensional α-Fe$_2$O$_3$ nanomaterials attract great attention due to their high surface areas (abundant active sites), excellent charge separation and potentially improved light absorption [16]. In addition, porous α-Fe$_2$O$_3$ materials have also been widely used to enhance the charge separation and improve the ptotocatalytic activity of α-Fe$_2$O$_3$ because pores enable shorter diffusion length that holes have to transfer by increasing interfacial area between electrolyte and semiconductor [17]. Particularly, the porous metal oxide nanotubes which combine the advantages of tubular 1D nanoarchitectures and porous structures can further enhance the performance of materials for photocatalysis [18]. However, the fabrication of porous α-Fe$_2$O$_3$ nanotubes with precisely tailored wall thickness, pore structure and crystallinity still remains a big challenge. On the other hand, forming junctions between different semiconductors is another effective strategy for promoting charge carriers migration and thus enhances the photo-conversion efficiency of semiconductors [9,19–21]. Wang's group constructed p-n junction by growing a thin layer of p-type Mg-doped hematite on the surface of n-type hematite, which was found to creat a built-in field that could facilitate the charge separation and boost the photocatalytic activity of hematite for photoelectrochemical water splitting [22]. Recently, Gong's group fabricated a Fe$_2$O$_3$ /Fe$_2$TiO$_5$ heterojunction photoanode via a hydrothermal method combined with atomic layer deposition. The heterojunction drived charge separation efficiently and the composite electrode presents a significantly enhanced photocurrent (1.63 mA cm^{-2} at 1.23 V versus RHE), which is 3.5 times that of the bare Fe$_2$O$_3$ electrode [12]. However, charges separated by the junction interface would still undergo severe recombination when transferred to the surface if the depth of the junction is too large [23]. Thus carefully designed α-Fe$_2$O$_3$ catalysts that simultaneously shorten charge carriers migration distance and speed up charge carriers transportation are urgently needed.

Atomic layer deposition (ALD) and molecular layer deposition (MLD) have been considered to be appealing technologies for constructing nanomaterials via a bottom-up approach with atomic or molecular level control, due to their self-limiting nature, excellent conformality, chemical selectivity and low reaction temperature [24–28]. By tuning the recipes of ALD and/or MID procedure, the composition, size or thickness, crystallinity and pore structure of the deposited nanomaterials could be easily tailored. In addition, ALD/MLD is known to permit the growth of composite materials with hetero- or homo-junctions [22]. More importantly, combination of ALD and MLD could fabricate new organic–inorganic hybrid materials, which not only matintain the beneficial aspects of each constituent but also exhibit some synergetic property [29]. Further more, the organic-inorgnic hybrid films are attractive precursors for the construction of porous functional metal oxide films with tunable thickness and pore size [25,30], which have been demonstrated to be promising in gas separation [31], stabilization of metal nanoparticles, [32] and catalytic materials [25,33]. However, the type and number of organic-inorganic films produced by MLD is still scarce because finding suitable coupling precursors and reactions is difficult [25,30]. To the best of our knowledge, no MLD process for Fe-hybrid films have been reported until now. Therefore, it is very desirable to develop novel MLD process to synthesize Fe-hybrid films with different organic fragments and resulting porous iron oxide films with controllable pore structure and junctions.

Herein, porous Fe$_2$O$_3$ nanotubes with controllable pore structure and phase junction have been synthesised by two novel MLD approachs using carbon nanofibers (CNFs) as template, based on two-step AB and four-step ACDC reaction sequences, respectively. The organic fractions of the Fe-hybrid MLD film not only act as soft templates to generate nanopores in nanotube walls but also play a key role in the formation of phase-junction. The porous structure and phase-junction significantly improve the charge separation efficiency, leading to a drastically increased photocatalytic activity for photo-Fenton reaction, and especially the porous α-γ Fe$_2$O$_3$ nanotubes produced by two-step AB MLD

from iron tert-butoxide (ITBT) and ethylene glycol (EG) exhibit the highest photocatalytic activity, which is more than a 6.5-fold and 20-fold improvement compared with the nonporous α-Fe$_2$O$_3$ nanotubes and commercial α-Fe$_2$O$_3$ nanoparticles, respectively.

2. Experimental section

2.1. Synthesis of P-Fe$_2$O$_3$-I nanotubes via two-step MLD process

P-Fe$_2$O$_3$-I nanotubes were prepared by template-assistant MLD method using CNFs (prepared by our previous method, for details, see the Supporting Information) as templates. MLD process was performed in a home-made ALD reactor (hot wall closed chamber type) with N$_2$ (99.999%) as both carrier and purging gas. Firstly, Fe-hybrid-I films were grown on the surface of CNFs via two-step MLD method using iron tert-butoxide (Fe$_2$(O^{t}Bu)$_6$) and EG as precursors. The deposition temperature was 120 °C. The precursors Fe$_2$(O^{t}Bu)$_6$ and EG were maintained at 100 °C and 65 °C, respectively. For each MLD cycle, the pulse time, exposure time, and purging time for Fe$_2$(O^{t}Bu)$_6$ and EG precursors were 3 s/15 s/25 s and 0.05 s/15 s/35 s, respectively. Afterwards, the samples were annealed at 500 °C in air atmosphere for 1 h and the P-Fe$_2$O$_3$-I nanotubes were obtained.

2.2. Synthesis of P-Fe$_2$O$_3$-II nanotubes via four-step MLD process

Firstly, Fe-hybrid-II films were grown on the surface of CNFs via four-step MLD method at 120 °C by sequential exposure of the CNFs to iron tert-butoxide (Fe$_2$(^{t}BuO)$_6$), ethanolamine, malonyl chloride and ethanolamine. The precursors Fe$_2$(O^{t}Bu)$_6$ and ethanolamine were maintained at 100 °C and 80 °C, respectively. For each MLD cycle, the pulse time, exposure time, and purging time for Fe$_2$(O^{t}Bu)$_6$, ethanolamine and malonyl chloride precursors were 3 s/15 s/25 s, 0.05 s/15 s/90 s, and 0.03 s/15 s/60 s, respectively. After the MLD process, the samples were annealed at 500 °C in air atmosphere for 1 h and the P-Fe$_2$O$_3$-II nanotubes were obtained.

2.3. Synthesis of NP-Fe$_2$O$_3$-I and NP-Fe$_2$O$_3$-II nanotubes via ALD process

NP-Fe$_2$O$_3$-I nanotubes were prepared by ALD method using iron tert-butoxide (Fe$_2$(O^{t}Bu)$_6$) and ultrapure water as precursors. The ALD reactor and the Fe$_2$(O^{t}Bu)$_6$ source were maintained at 120 and 100 °C, respectively. For each ALD cycle, the pulse time, exposure time, and purging time for Fe$_2$(O^{t}Bu)$_6$ and H$_2$O precursors were 3 s/15 s/25 s and 0.02 s/15 s/25 s, respectively. Afterwards, the obtained Fe$_2$O$_3$/CNFs were transferred to a furnace and annealed at 500 °C in air atmosphere for 1 h and the NP-Fe$_2$O$_3$-I nanotubes were obtained. NP-Fe$_2$O$_3$-II nanotubes were synthesized by a similar method, just using PVA nanofibers (see the Supporting Information) instead of CNFs as template, which were removed selectively by dissolving in hot water at 90 °C prior to anneal process

2.4. Characterization

The thicknesses of Fe-hybrid films were measured using an X-ray reflectivity (XRR) instrument (PANalytical, X´Pert PRO). X-ray powder diffraction analyses (XRD; X´Pert PRO, PANalytical) were performed to examine the crystallinity of the obtained iron oxide samples. In situ XRD patterns were collected on a D8 Advance diffractometer (Bruker). To trace the phase changes of the samples, 100 mg of Fe-hybrid-I/CNFs was loaded into the in situ cell and calcined under air (20 mL min^{-1}) with a heating step at 5 °C min^{-1}, which was stopped at certain temperature values for 15 min to record the XRD pattern. Transmission electron microscopy (TEM) and High-resolution transmission electron microscopy (HRTEM) images were characterized by a JEOL-2100 F microscope. FTIR (PerkinElmer, Frontier FT-IR) spectroscopy was used to investigate the chemical composition of the Fe-hybrid samples. The

spectrum of substrate (Si wafer) was subtracted from the spectra of the Fe-hybrid films to rule out the effect of the substrate (Piranha-cleaned silicon substrate was used as a background reference for FT-IR measurements). The X-ray photoelectron spectra (XPS) were conducted on an AXIS ULTRA DLD photoelectron spectrometer (Al Kα source, 1486.6 eV). The surface area of the iron oxide nanotubes was evaluated from N_2 adsorption isotherms (Micromeritics ASAP 2020 Plus automated characterization system). UV–vis diffused reflectance spectra of iron oxides samples were recorded on a UV–vis spectrophotometer (Thermo Scientific Evolution 220). Photoluminescence (PL) spectra were performed at room temperature (F-7000, Hitachi, Japan). The excitation wavelength was fixed at 251 nm.

2.5. Photo-Fenton catalytic activity tests

The photocatalytic activities of the obtained iron oxide nanotubes were tested based on the photo-Fenton degradation of rhodamine B (RhB) solution under visible-light irradiation. Typically, 2.5 mg of the iron oxide nanotubes was mixed with 30 mL of RhB solution ($10\,mg\,L^{-1}$) under stirring. After keeping stirring for 1 h in the dark to ensure an adsorption/desorption equilibrium of RhB, 200 μL of hydrogen peroxide (H_2O_2, 30 wt.%, Aldrich) was injected into the mixture under stirring. Then the suspension was irradiated by a Xenon lamp ($\lambda \geq 420$ nm, CEL-HXF300, Beijing CEAULIGHT Co. Ltd.). At regular time intervals, ~1.5 ml of the suspension were taken out and centrifuged at $12\,000\,r\,min^{-1}$ for 10 min. Then the liquid supernatant were detected using UV–vis measurements (NanoDrop 2000c, Thermo Scientific) to monitor the concentration of RhB at different reaction time.

3. Results and discussion

In order to fabricate porous iron oxide films with controlled pore size and thickness, two novel MLD processes (labeled as MLD-I and MLD-II, respectively) are firstly developed in here to synthesize two kinds of new Fe-hybrid films with different organic constituents (denoted as Fe-hybrid-I and Fe-hybrid-II, respectively), which hereafter are used as precursors for producing porous iron oxide nanotubes. Fig. 1a presents a proposed reaction sequence during the two-step AB MLD-I process for growth of Fe-hybrid-I films from ITBT (precursor A) and EG (precursor B), that is, ITBT firstly reacts with hydroxyl groups on the substrate surface to yield an tert-butoxide-terminated surface, which in turn reacts with EG in the next step and reforms a hydroxyl-terminated surface. One single MLD-I cycle consists of the two-step doses of ITBT and EG. The two-step AB sequence is repeated until a desired film thickness was obtained. In contrast, the MLD-II process involves dosing ITBT (precursor A), ethanolamine (EA, precursor C), and malonyl chloride (MC, precursor D) in a four-step ACDC sequence, as shown in Fig. 1b. Briefly, ITBT firstly reacts with hydroxyl groups on the substrate surface to form a new surface species terminated by tert-butoxide. Subsequently, the tert-butoxide species react preferentially with the hydroxyl end of the EA to generate an amine-terminated surface, which then attaches the MC to form acyl chloride surface species. In the final step, the surface-terminating acyl chloride groups react preferentially with the amino end of the EA to regenerate hydroxyl groups on the surface, finishing one MLD-II cycle. The four-step ACDC sequence is then repeated in a desired number by exposure to ITBT, EA, MC and EA to grow the Fe-hybrid-II films. Ex situ X-ray reflectivity (XRR) analysis revealed that the growth rate of Fe-hybrid-I and Fe-hybrid-II films on Si substrate under the optimized deposition conditions (for details, see the experimental section) were about 0.9 and 2.1 Å per MLD cycle, respectively. FT-IR analysis was used to probe the chemical bonding and composition of the as-synthesized Fe-hybrid MLD films. In the FT-IR spectrum of Fe-hybrid-I film (Fig. 2a), the absorbance peaks observed at 2946 and $2862\,cm^{-1}$ can be ascribed to CH_2 asymmetric and symmetric stretching vibrations. Absorbance peaks
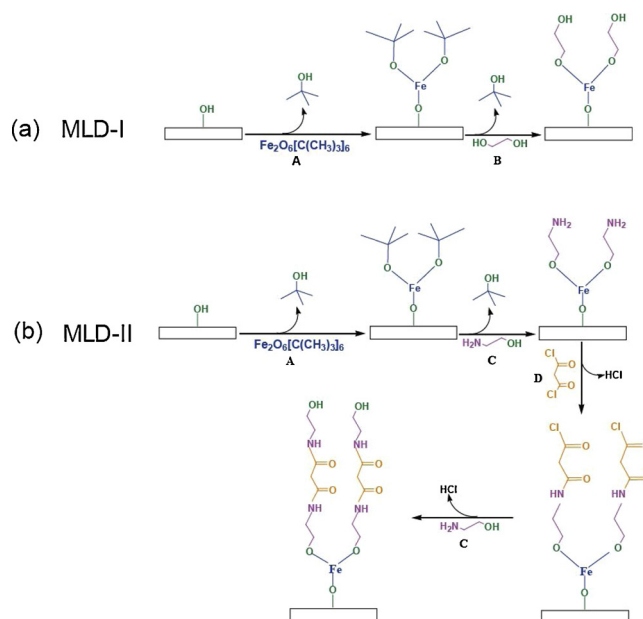

Fig. 1. (a) Schematic diagram for the synthesis of Fe-hybrid-I film via two-step AB MLD-I process using iron tert-butoxide (ITBT, precursor A) and ethylene glycol (EG, precursor B) as precursors; (b) Schematic diagram for the growth of Fe-hybrid-II film via four-step ACDC MLD-II process using ITBT (precursor A), ethanolamine (EA, precursor C), and malonyl chloride (MC, precursor D) as precursors.
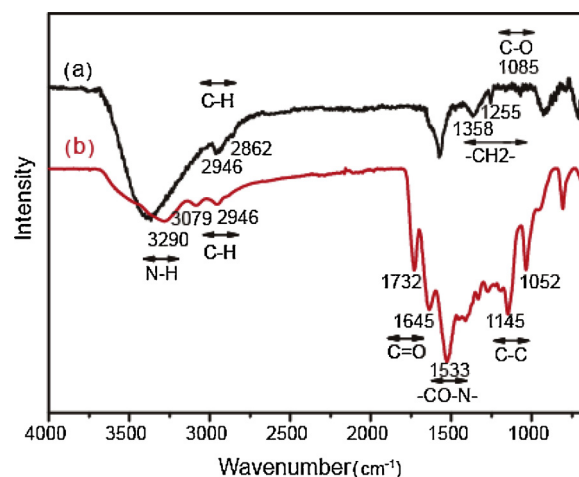

Fig. 2. FT-IR spectra of (a) Fe-hybrid-I film and (b) Fe-hybrid-II film obtained by applying 300 AB and ACDC MLD cycles, respectively.

from CH_2 scissoring and twisting are also monitored at 1200-1400 cm^{-1}. In addition, the C—O stretching vibration is observed at 1085 cm^{-1} [29,34]. The above-mentioned results are indicative of successful incorporation of organic constituent ($-OCH_2-CH_2O-$) into the film. For the Fe-hybrid-II film (Fig. 2b), the absorbance peaks observed at 2750–3100 and 3160–3420 can be ascribed to C—H and N—H stretching vibrations, respectively [25,35]. The C=O stretching vibration at 1645 cm^{-1}, and CO-N-H bending modes at 1533 cm^{-1} are also detected.[25] At low frequencies, two noticeable peaks at 1145 and 1052 cm^{-1} can be assigned to C—C and C—O vibrations, respectively. These results verify the successful covalent bonding of EA and MC to form the new Fe-hybrid-II film via the ACDC four-step MLD processes.

These aforementioned Fe-hybrid films with controllable length of carbon chains provide versatile routes to create porous iron oxide nanotubes with tunable pore sizes and wall thicknesses. The overall synthesis of porous Fe_2O_3 nanotubes is schematically illustrated in
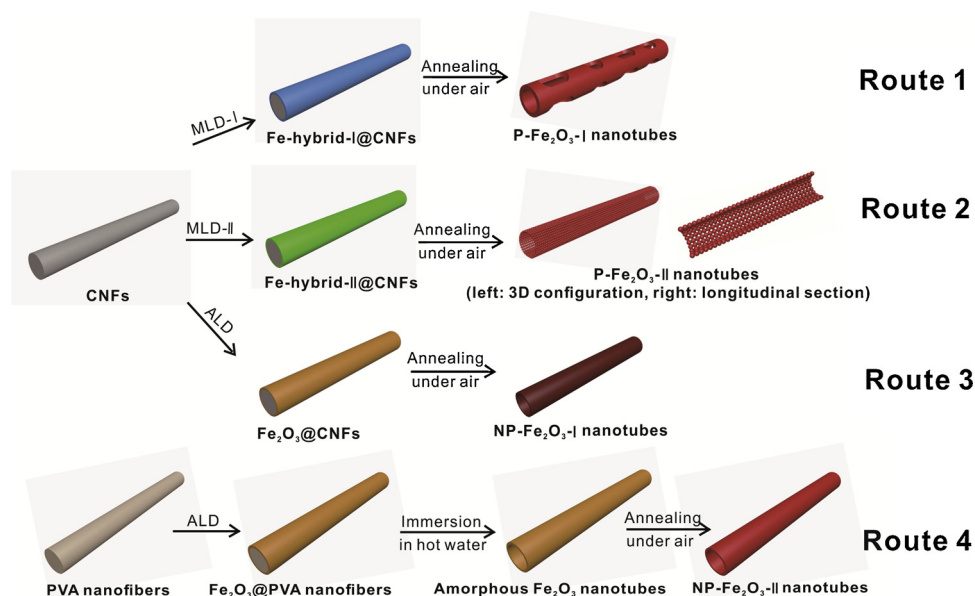
Fig. 3. Schematic illustration of the procedure for the fabrication of porous (route 1 and 2) and non-porous (route 3 and 4) Fe$_2$O$_3$ nanotubes via MLD or ALD technology.

Table 1
Four different Fe$_2$O$_3$ nanotubes prepared by 300 MLD or ALD cycles and their physicochemical properties.

Samples	Templates	Preparation method	Pore structure	Phase composition	Surface areas ($m^2 g^{-1}$)
P-Fe$_2$O$_3$-I	CNFs	MLD-I, Route 1	porous	α-Fe$_2$O$_3$, γ-Fe$_2$O$_3$	45.3
P-Fe$_2$O$_3$-II	CNFs	MLD-II, Route 2	porous	α-Fe$_2$O$_3$, γ-Fe$_2$O$_3$	51.4
NP-Fe$_2$O$_3$-I	CNFs	ALD, Route 3	nonporous	α-Fe$_2$O$_3$, Fe$_3$O$_4$	35.4
NP-Fe$_2$O$_3$-II	PVA nanofibers	ALD, Route 4	nonporous	α-Fe$_2$O$_3$,	36.3

Fig. 3. Firstly, Fe-hybrid films were deposited onto CNFs by different MLD process (route 1 and route 2). Then the as-prepared Fe-hybrid/CNFs were annealed at 500 °C in air atmosphere to remove the organic constituents and CNFs, giving rise to porous Fe$_2$O$_3$ nanotubes with controllable pore structures (denoted as P-Fe$_2$O$_3$-I and P-Fe$_2$O$_3$-II, corresponding to route 1 and route 2, respectively, Table 1). For comparison, two kinds of non-porous Fe$_2$O$_3$ nanotubes (NP-Fe$_2$O$_3$-I and NP-Fe$_2$O$_3$-II) were also prepared by ALD process (Figure S1) from ITBT and water using CNFs (route 3) and electrospun PVA nanofibers (route 4, the process of fabrication of electrospun PVA nanofibers see the Supporting Information) as templates, respectively. It should be note, prior to annealing step, Fe$_2$O$_3$/PVA nanofibers in the route 4 were immersed in hot water (90–100 °C) to dissolve the PVA nanofibers.

TEM and HRTEM were used to confirm the morphology and crystal phase of the obtained Fe$_2$O$_3$ nanotubes. Fig. 4a, 4c and 4e show the TEM images of Fe$_2$O$_3$ nanotubes produced via route 1, route 2 and route 4, respectively. It can be seen that all the three Fe$_2$O$_3$ specimens have a well-defined nanotubes-like morphology with a wall thickness of about 23, 21, and 20 nm, respectively. For the P-Fe$_2$O$_3$-I nanotubes produced by 300 MLD cycles from ITBT and EG, nanopores can be clearly observed in its walls, though the size and shape of the pores are inhomogenous. In stark contrast, uniformly distributed nanopores exist in the walls of P-Fe$_2$O$_3$-II nanotubes produced by 300 MLD cycles from ITBT, EA and MC (Fig. 4c). The difference in pore structure between these two type of Fe$_2$O$_3$ nanotubes may be ascribed to the different organic spacers. The glycol between the Fe ions in Fe-hybrid-I film is too short to prevent the aggregation and coalescence of Fe$_2$O$_3$ nanoparticles at high temperatures through Ostwald ripening, leading to the partial collapse and fusion of the pores, while the organic spacer in Fe-hybrid-II film is relatively long (Fig. 1), which can act as soft template to generate nanopores uniformly distributed in the wall of the Fe$_2$O$_3$
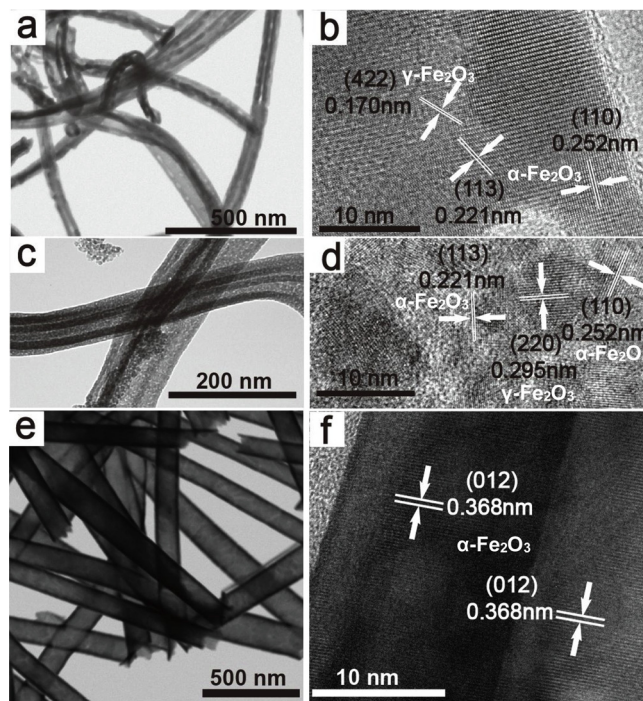

Fig. 4. TEM and HRTEM images of P-Fe$_2$O$_3$-I (a and b), P-Fe$_2$O$_3$-II (c and d) and NP-Fe$_2$O$_3$-II (e and f) nanotubes. The numbers of the MLD or ALD cycles for Fe-hybrid or Fe$_2$O$_3$ are all 300.
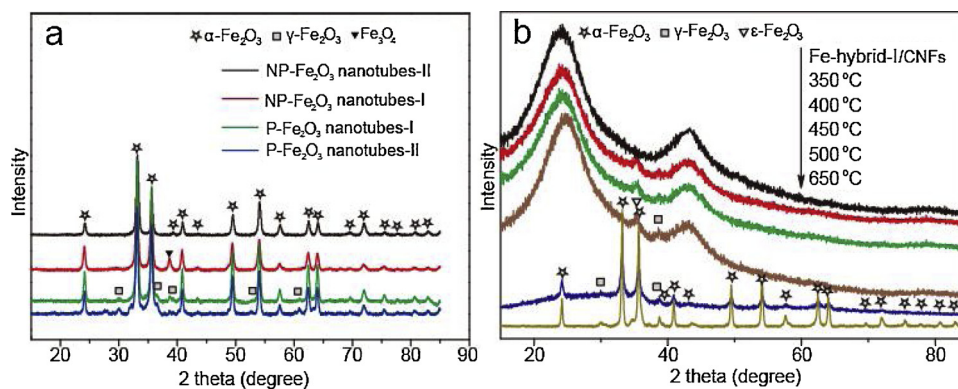
Fig. 5. (a) XRD patterns of different Fe_2O_3 nanotube samples obtained from 300 MLD or ALD cycles. (b) XRD patterns of Fe-hybrid-I/CNFs calcined at different temperatures (The numbers of the MLD cycles for Fe-hybrid-I is 300).

nanotubes. Compared to MLD process, the ALD process using ITBT and H_2O as sources only generates nonporous Fe_2O_3 nanotubes with smooth surface. The generation of nanopores in the wall of Fe_2O_3 nanotubes make the surface area of P-Fe_2O_3-I (45.3 $m^2 g^{-1}$, Table 1 and Figure S3) and P-Fe_2O_3-II (51.4 $m^2 g^{-1}$) be higher than that of NP-Fe_2O_3-II (36.3 $m^2 g^{-1}$), facilitating mass/charge transfer across the catalyst-electrolyte interface. Fig. 4b, 4d and 4f display the HRTEM images of P-Fe_2O_3-I, P-Fe_2O_3-II and NP-Fe_2O_3-II, respectively. The distance between adjacent lattice fringes of the NP-Fe_2O_3-II is 0.368 nm (Fig. 4f), which is in coincidence with the lattice spacing of the (012) planes of α-Fe_2O_3 and no other crystal phases are detected. Interestingly, besides α-Fe_2O_3, γ-Fe_2O_3 phase also exists in both P-Fe_2O_3-I (Fig. 4b) and P-Fe_2O_3-II (Fig. 4d), resulting in the formation of α-γ phase junctions, which are expected to promote charge separation and transfer.

The crystal structures of the as-prepared iron oxide nanotubes were further studied by XRD as displayed in Fig. 5a. For P-Fe_2O_3-I and P-Fe_2O_3-II, apart from a-Fe_2O_3 crystalline signals (JCPDS card number 33-0664), several weak diffraction peaks, belonged to γ-Fe_2O_3 phase (JCPDS card number 39–1346), can be detected, indicating that a- and γ-phase Fe_2O_3 coexiste in both P-Fe_2O_3-I and P-Fe_2O_3-II. For NP-Fe_2O_3-II, all the diffraction peaks could be indexed to a-Fe_2O_3, and no characteristic peaks from other crystalline polymorphs of Fe_2O_3 (β-Fe_2O_3, γ-Fe_2O_3, and ε-Fe_2O_3) can be observed. These results are in good accordance with HRTEM results.

The formation of Fe_2O_3 nanotubes with α-γ phase junctions under annealing at a temperature as high as 500 °C is surprising because γ-Fe_2O_3 is thermodynamically unstable and usually tend to be converted to α-Fe_2O_3 when the temperature exceeds a threshold value (~400 °C) [36]. In order to understand the formation mechanism of porous Fe_2O_3 nanotubes with α-γ phase junctions, we carried out in situ high-temperature XRD examinations to provide deep insight on the formation of α-γ phase junctions during the thermal treatment in air atmosphere from room temperature to 650 °C, taking Fe-hybrid-I/CNFs for example. As shown in Fig. 5b, before thermal annealing, the as-prepared Fe-hybrid-I/CNFs presented two broad diffraction peaks at around 24.0° and 43.0°, which correspond to the (111) and (010) facets of graphitic carbon of CNFs substrates, respectively [37]. No distinct peaks related to iron oxides were observed, indicating the amorphous nature of the Fe-hybrid-I films. As the annealing proceeded, Fe-hybrid-I films decomposed gradually and crystalline iron oxide began to formed. At 350 °C, two new weak peaks related to ε-Fe_2O_3 [38] and γ-Fe_2O_3 were observed at 35.4° and 38.8°, respectively. This phenomenon is consistent with many previous reports, in which γ-Fe_2O_3 were synthesized by thermal decomposition of appropriate iron-containing compounds such as iron(III) hydroxide caprylate, gluconate dihydrate, iron(II) oxalate dihydrate, or iron(II) acetonacetate [36]. With an increased annealing temperature to 400 °C and 450 °C, ε-Fe_2O_3 and γ-Fe_2O_3 remained and no new iron oxide phase occured. When the temperature

further increased to 500 °C, the ε-Fe_2O_3 reflections disappeared and α-Fe_2O_3 phase formed because the readily transformation of ε-Fe_2O_3 to α-Fe_2O_3 upon heating. However, the γ-Fe_2O_3 phase still remained, leading to the formation of α-γ phase junctions in the Fe_2O_3 nanotubes, though γ-Fe_2O_3 is also thermodynamically unstable at elevated temperatures and suffers from an irreversible transformation to α-Fe_2O_3. It should be noted that the α- and γ-Fe_2O_3 still coexist in the Fe_2O_3 nanotubes even at 650 °C. In previous reports, the γ-Fe_2O_3-to-α-Fe_2O_3 could be controlled by tuning the degree of agglomeration of the ferric oxide particles and the scope for particle growth phase transformation [36]. Herein, using MLD method, we could easily obtained CNFs supported Fe-hybrid films composed with Fe ion and organic constituents, which were firstly transfered to ferric oxide/CNFs with porous structure at the initial stage of annealing process. This porous structure could impede the particles' growth and enhanced the stability of γ-Fe_2O_3, resulting in the formation of α-γ phase junctions at relatively high temperatures. Therefore, we assumed that the role of organic constituents in the Fe-hybrid film was very critical in the formation of α-γ phase junctions. To verify this, additional experiments were performed. In a control experiments, Fe_2O_3/CNFs without organic constituents were prepared by ALD process from ITBT and water using CNFs as templates (Fig. 3, route 3), After annealing at 500 °C in air atmosphere for 1 h, nonporous Fe_2O_3 nanotubes (NP-Fe_2O_3-I) with α-Fe_2O_3-Fe_3O_4 heterojunction were obtained and no γ-Fe_2O_3 phase was obviously observed, as confirmed by TEM (Figure S2a), HRTEM (Figure S2b), XRD (Fig. 5a) and XPS (Figure S4) analyses. The formation of minute amount of Fe_3O_4 in the nonporous Fe_2O_3 nanotubes could be ascribed to the reductive ability of the CNFs. To rule out the effect of CNFs, we further prepared nonporous iron oxide nanotubes (NP-Fe_2O_3-II) by ALD process from ITBT and water using electrospun PVA nanofibers as templates, which were removed selectively by dissolving in hot water at 90 °C prior to anneal process (Fig. 3, route 4). As expected, only α-Fe_2O_3 phase was detected by HRTEM (Fig. 4f) and XRD (Fig. 5a) analyses, indicating the amorphous ALD iron oxide nanotubes were completely transformed to pure α-Fe_2O_3 nanotubes under the same annealing conditions. These results unmistakably demonstrated that the organic fractions of the Fe-hydrid MLD films play a key role in the generation of α-γ phase junctions during annealing process.

The optical properties of the Fe_2O_3 nanotubes were investigated by UV–vis spectroscopy, as represented in Fig. 6a. It can be seen that all the Fe_2O_3 nanotube samples show a comparable adsorption edge around 600 nm, indicating that the formation α-γ phase junctions or α-Fe_2O_3-Fe_3O_4 heterojunction on Fe_2O_3 nanotubes has little affect on its adsorption ability. It is well-known that forming a junction structure can promote efficient electron-hole separation and therefore to improve the photocatalytic performance of the α-Fe_2O_3 nanotubes. Photoluminescence (PL) experiments were employed to measure the charge transport and separation properties of the as-prepared Fe_2O_3
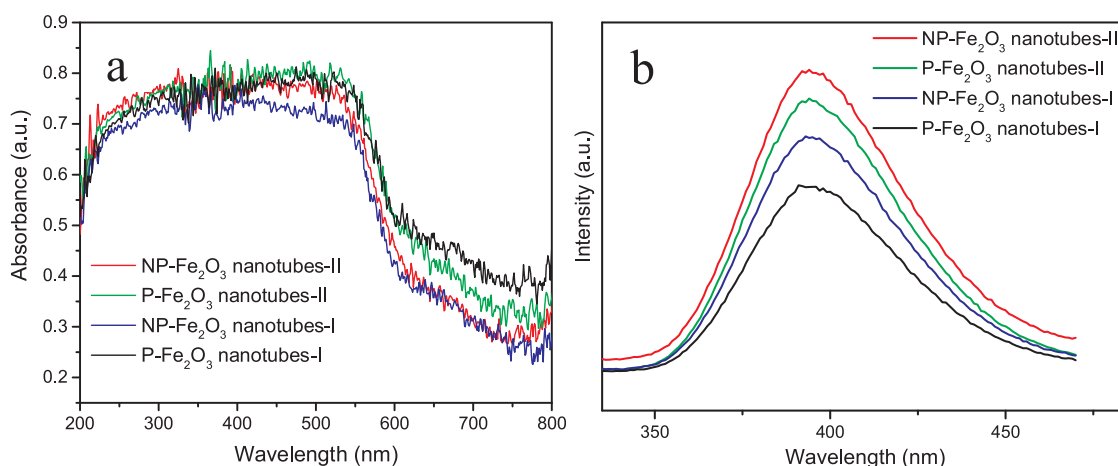
Fig. 6. (a) UV–vis spectra and (b) PL spectra of different Fe$_2$O$_3$ nanotube samples obtained from 300 MLD or ALD cycles.

nanotubes. As shown in Fig. 6b, the Fe$_2$O$_3$ nanotube samples all show a broad photoluminescence peak centered at around 395 nm, which is derived from the recombination of the band-gap photo-excited electron-hole pairs. The emission intensity of the Fe$_2$O$_3$ nanotubes decrease by forming α-γ phase junctions or α-Fe$_2$O$_3$-Fe$_3$O$_4$ heterojunctions, indicating that charge transport and separation can be greatly improved by forming α-γ phase junctions or α-Fe$_2$O$_3$-Fe$_3$O$_4$ heterojunctions. In addition, the emission intensity of P-Fe$_2$O$_3$-II is higher than that of P-Fe$_2$O$_3$-I and NP-Fe$_2$O$_3$-I, which is presumably due to electron-hole recombination across grain boundaries between nanoparticles in the walls of P-Fe$_2$O$_3$-IInanotubes.

The porous structures and α-γ phase junctions of the obtained Fe$_2$O$_3$ nanotubes would benefit mass/charge transport and thus facilitate the catalytic kinetics. Photo-Fenton catalysis is a technologically promising solar-driven process in wastewater treatment. The photocatalytic activities of the as-prepared Fe$_2$O$_3$ nanotubes with different pore structures and phase composition were evaluated for rhodamine B (RhB) photodegradation in the presence of H$_2$O$_2$ under visible-light illumination (λ ≥ 420 nm). Firstly, the influence of the wall thickness (determined by the MLD cycle numbers inhere) of the Fe$_2$O$_3$ nanotubes on their photocatalytic behavior was investigated. As shown in Fig. 7, both P-Fe$_2$O$_3$-I and P-Fe$_2$O$_3$-II samples exhibit a hump-like photocatalytic activity depending on the MLD cycles numbers (with 300 MLD cycles as an optimal amount for both P-Fe$_2$O$_3$-I and P-Fe$_2$O$_3$-II). This phenomenon can be reasonably explained as that the increment of MLD cycle

numbers will enhance the light absorption of Fe$_2$O$_3$ nanotubes but also lead to more electron-hole recombination because of longer carriers diffusion distance, and thus, it should appear an optimal balance between these two contradictory factors at a certain MLD cycle numbers.

Next, the validity of porous structures and α-γ phase junctions on improving photocatalytic efficiency were investigated, as shown in Fig. 8. Obviously, the degradation rate of RhB by P-Fe$_2$O$_3$-I, P-Fe$_2$O$_3$-II and NP-Fe$_2$O$_3$-I were much faster than those of NP-Fe$_2$O$_3$-II and commercial α-Fe$_2$O$_3$ nanoparticles (Aldrich, average size < 50 nm) at the same exposure time. The corresponding degradation efficiencies were about 99%, 88%, 94%, 45% and 21% after 15 min irradiation with P-Fe$_2$O$_3$-I, P-Fe$_2$O$_3$-II, NP-Fe$_2$O$_3$-I, NP-Fe$_2$O$_3$-II and commercial α-Fe$_2$O$_3$ nanoparticles, respectively (Fig. 8a). In addition, only minor degradation (6.9% in 20 min) was observed in a blank test (without catalyst). For comparison, the catalytic activity of P-Fe$_2$O$_3$-I was also test in the dark and only 13.2% RhB can be degraded after 15 min, demonstrated that the Fenton reaction on P-Fe$_2$O$_3$-I could be greatly accelerated by visible-light irradiation. To evaluate the reactivity of Fe$_2$O$_3$ nanotubes catalysts quantitatively, the apparent reaction rate constant (k) of RhB degradation was calculated, and the results are shown in Fig. 8b. It can be seen that P-Fe$_2$O$_3$-I shows the highest k value (0.282 min^{-1}), which is approximately 6.5-fold larger than that of the nonporous α-Fe$_2$O$_3$ nanotubes (NP-Fe$_2$O$_3$-II) and 20 times larger than that of the commercial α-Fe$_2$O$_3$ nanoparticles. Compared these activity results (P-Fe$_2$O$_3$-I > NP-Fe$_2$O$_3$-I > P-Fe$_2$O$_3$-II > NP-Fe$_2$O$_3$-II) with above-
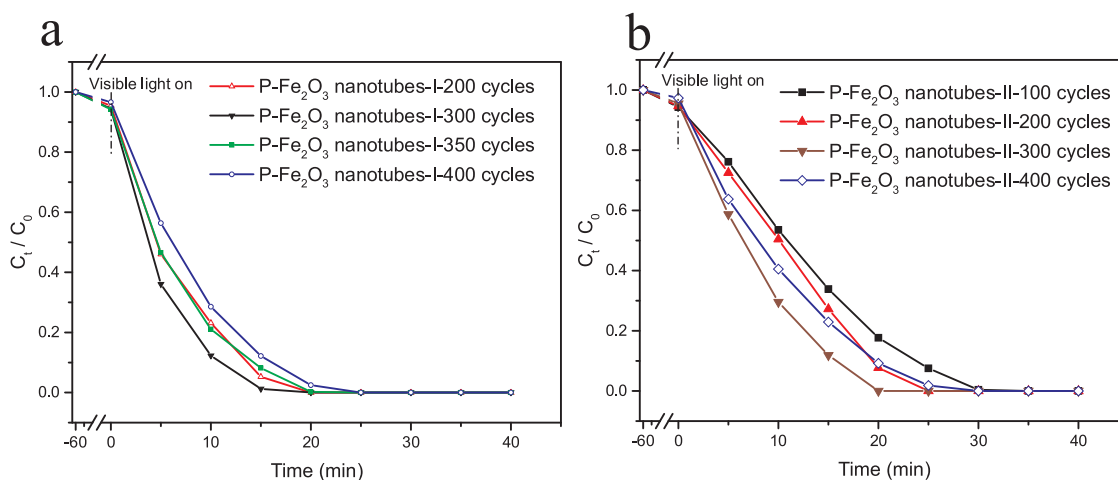

Fig. 7. Photodegradation of RhB on (a) P-Fe$_2$O$_3$-I and (b) P-Fe$_2$O$_3$-II produced with varying MLD cycles under visible-light irradiation in the presence of H$_2$O$_2$ additive. Reaction conditions: RhB concentration 10 mg L^{-1}, catalyst concentration 0.08 g L^{-1}, H$_2$O$_2$ molar concentration 66.7 mM, initial pH 7.2, 300 W Xe-lamp (λ > 420 nm).
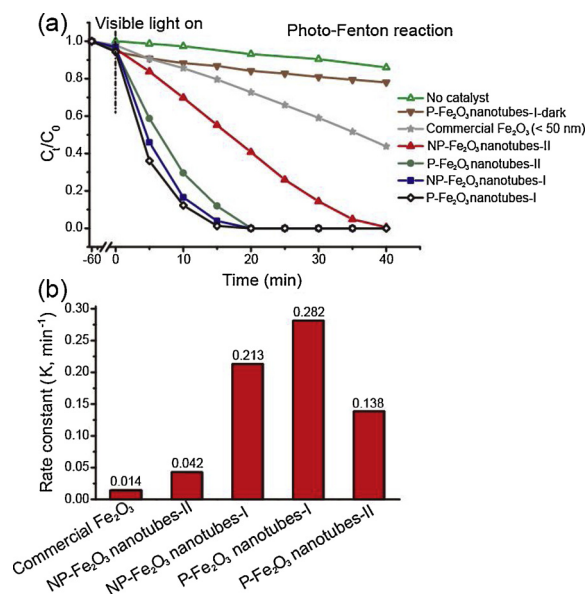
Fig. 8. (a) Photodegradation of RhB on different a-Fe$_2$O$_3$ nanotubes (produced with 300 MLD or ALD cycles) under visible-light irradiation in the presence of H$_2$O$_2$ additive. Reaction conditions: RhB concentration 10 mg L^{-1}, catalyst concentration 0.08 g L^{-1}, H$_2$O$_2$ molar concentration 66.7 mM, initial pH 7.2, 300 W Xe-lamp (λ > 420 nm). (b) Rate constants of RhB degradation on different a-Fe$_2$O$_3$ nanotubes based on pseudo-first-order kinetic model.

mentioned specific surface area results (P-Fe$_2$O$_3$-II > P-Fe$_2$O$_3$-I > NP-Fe$_2$O$_3$-II ≈ NP-Fe$_2$O$_3$-I), it is unambiguously demonstrated that both the porous structure and phase composition (phase junction and heterojunction) have significant impacts on the photocatalytic performance of Fe$_2$O$_3$ nanotubes. The superior photocatalytic performance of P-Fe$_2$O$_3$-I is attributed to its relative high specific surface area and the highest charge separation efficiency owing to the α-γ phase junctions and small amount of grain boundaries.

Due to the dye self-sensitization process may also occur under visible light irradiation, we performed the wavelength dependence of the photocatalysis tests to further study the photocatalytic activities of P-Fe$_2$O$_3$-I nanotubes (Figure S5a). It can be seen that the photocatalytic activity of Fe$_2$O$_3$-I correlates well with its absorption spectrum, indicating semiconductor photocatalysis dominates the RhB photodegradation process and RhB dye self-sensitization is not obvious at this condition. In addition, we also investigated the photocatalytic performance of P-Fe$_2$O$_3$-I for the degradation of 4-nitrophenol (4-NP) because the 4-NP is more stable and only absorb UV lights, which could rule out the effect of dye self-sensitization under visible light irradiation. As shown in Figure S5b, the P-Fe$_2$O$_3$-I exhibits higher photocatalytic activity than NP-Fe$_2$O$_3$-II for 4-NP degradation, that is, 99% and 58% of 4-NP were degraded under visible light irradiation for 60 min, respectively. These results further confirm that the porous structure and phase-junction of P-Fe$_2$O$_3$-I facilitate the charge separation efficiency and photocatalytic activity of iron oxide nanotubes.

As we know, Fe$_2$O$_3$ is a classic Fenton-like reagent, which could catalyze the dissociation of hydrogen peroxide to generate highly reactive radicals, which then attack and destroy the organic pollutants. To study the underlying photodegradation mechanism of RhB over P-Fe$_2$O$_3$-I nanotubes, the effects of various radical scavengers on the degradation of RhB were studied. Benzoquinone (BQ) and tert-Butyl alcohol (TBA) were used as ˙O^{2-} and ˙OH scavengers, respectively. As shown in Figure S6, the photodegradation rate of RhB remains unchanged after the addition of BQ, indicating that ˙O^{2-} was not the main reactive species. By contrast, a severe suppression of the degradation rate of RhB was observed after the additionof TBA, implying that ˙OH radical is dominant responsible for this heterogeneous photo-Fenton

reaction on P-Fe$_2$O$_3$-I nanotubes.

According to the above results and discussion, a possible photo-Fenton reaction mechanism over porous Fe$_2$O$_3$ nanotubes with α-γ phase junction was proposed, as shown in Figure S7. Under visible light irradiation, Fe$_2$O$_3$ is firstly excited and electrons and holes are generated. The photoinduced carriers are then efficiently separated and migrate to the surface due to the porous nanotubular structure and α-γ phase junction. Subsequently, the electrons and holes that reach the surface react with H$_2$O$_2$ and H$_2$O respectively to generate high active ˙OH radical. Finally, under the attack of ˙OH, RhB was decomposed and mineralized to H$_2$O and CO$_2$.

4. Conclusion

In summary, we have developed two new MLD approaches to synthesize two kinds of Fe-hybrid films with different organic constituents based on two-step AB and four-step ACDC reaction sequences, respectively. Under annealing, the Fe-hybrid films/CNFs could converted into porous Fe$_2$O$_3$ nanotubes with controllable pore size and α-γ phase junction. The organic fractions of the Fe-hybrid MLD film not only act as soft templates to generate nanopores in nanotube walls but also play a key role in the formation of phase-junction. The porous structure and phase-junction significantly improve the charge separation and transfer. As a result, the porous Fe$_2$O$_3$ nanotubes exhibited superior activities for photo-Fenton reaction, and especially the porous α-γ Fe$_2$O$_3$ nanotubes produced by two-step AB MLD from iron tert-butoxide (ITBT) and ethylene glycol (EG) exhibit the highest photocatalytic activity, which is more than a 6.5-fold and 20-fold improvement compared with the nonporous pure phase α-Fe$_2$O$_3$ nanotubes and commercial α-Fe$_2$O$_3$ nanoparticles, respectively. The MLD methods described here provides a new bottom-up approach to develop nanoporous Fe$_2$O$_3$ based materials with controllable pore size and crystalline structure.

Appendix A. Supplementary data

Supplementary material related to this article can be found, in the online version, at doi:https://doi.org/10.1016/j.apcatb.2019.02.029.

References

[1] T.C. Kaspar, D.K. Schreiber, S.R. Spurgeon, M.E. McBriarty, G.M. Carroll, D.R. Gamelin, S.A. Chambers, Adv. Mater. 28 (8) (2016) 1616–1622.
[2] Y. Lin, S. Zhou, S.W. Sheehan, D. Wang, J. Am. Chem. Soc. 133 (8) (2011) 2398–2401.
[3] L. Wang, N.T. Nguyen, X. Huang, P. Schmuki, Y. Bi, Adv Funct. Mater. (2017) 1703527.
[4] J. Qu, Y. Yu, C.-Y. Cao, W.-G. Song, Chem. A Eur. J. 19 (34) (2013) 11172–11177.
[5] S.C. Warren, K. Voïtchovsky, H. Dotan, C.M. Leroy, M. Cornuz, F. Stellacci, C. Hébert, A. Rothschild, M. Grätzel, Nat. Mater. 12 (9) (2013) 842–849.
[6] T. Hisatomi, H. Dotan, M. Stefik, K. Sivula, A. Rothschild, M. Grätzel, N. Mathews, Adv. Mater. 24 (20) (2012) 2699–2702.
[7] Y. Zhang, S. Jiang, W. Song, P. Zhou, H. Ji, W. Ma, W. Hao, C. Chen, J. Zhao, Energy Environ. Sci. 8 (4) (2015) 1231–1236.
[8] H.-J. Ahn, K.-Y. Yoon, M.-J. Kwak, J.-H. Jang, Angew. Chem. Int. Ed. 55 (34) (2016) 9922–9926.
[9] P.S. Bassi, R.P. Antony, P.P. Boix, Y. Fang, J. Barber, L.H. Wong, Nano Energy 22 (2016) 310–318.
[10] C. Li, A. Li, Z. Luo, J. Zhang, X. Chang, Z. Huang, T. Wang, J. Gong, Angew. Chem. Int. Ed. 56 (15) (2017) 4150–4155.
[11] G. Wang, Y. Ling, D.A. Wheeler, K.E.N. George, K. Horsley, C. Heske, J.Z. Zhang,

Y. Li, Nano Lett. 11 (8) (2011) 3503–3509.

[12] C. Li, T. Wang, Z. Luo, S. Liu, J. Gong, Small 12 (25) (2016) 3415–3422.

[13] H. Gao, C. Liu, H.E. Jeong, P. Yang, ACS Nano 6 (1) (2012) 234–240.

[14] J. Zhu, Z. Yin, D. Yang, T. Sun, H. Yu, H.E. Hoster, H.H. Hng, H. Zhang, Q. Yan, Energy Environ. Sci. 6 (3) (2013) 987–993.

[15] G.K. Mor, H.E. Prakasam, O.K. Varghese, K. Shankar, C.A. Grimes, Nano Lett. 7 (8) (2007) 2356–2364.

[16] S. Xie, Q. Zhang, G. Liu, Y. Wang, Chem. Commun. 52 (1) (2016) 35–59.

[17] J. Brillet, M. Grätzel, K. Sivula, Nano Lett. 10 (10) (2010) 4155–4160.

[18] Q. Wei, F. Xiong, S. Tan, L. Huang, E.H. Lan, B. Dunn, L. Mai, Adv. Mater. 29 (20) (2017) 1602300.

[19] X. Wang, Q. Xu, M. Li, S. Shen, X. Wang, Y. Wang, Z. Feng, J. Shi, H. Han, C. Li, Angew. Chem. Int. Ed. 51 (52) (2012) 13089–13092.

[20] P. Zhang, T. Wang, X. Chang, J. Gong, Acc. Chem. Res. 49 (5) (2016) 911–921.

[21] Y. Fang, Y. Ma, X. Wang, Chin. J. Catal. 39 (3) (2018) 438–445.

[22] Y. Lin, Y. Xu, M.T. Mayer, Z.I. Simpson, G. McMahon, S. Zhou, D. Wang, J. Am. Chem. Soc. 134 (12) (2012) 5508–5511.

[23] A. Li, X. Chang, Z. Huang, C. Li, Y. Wei, L. Zhang, T. Wang, J. Gong, Angew. Chem. Int. Ed. 55 (44) (2016) 13734–13738.

[24] K. Gregorczyk, M. Knez, Prog. Mater. Sci. 75 (2016) 1–37.

[25] C. Chen, P. Li, G. Wang, Y. Yu, F. Duan, C. Chen, W. Song, Y. Qin, M. Knez, Angew. Chem. Int. Ed. 52 (35) (2013) 9196–9200.

[26] Z. Gao, M. Dong, G. Wang, P. Sheng, Z. Wu, H. Yang, B. Zhang, G. Wang, J. Wang, Y. Qin, Angew. Chem. Int. Ed. 54 (31) (2015) 9006–9010.

[27] H. Ge, B. Zhang, X. Gu, H. Liang, H. Yang, Z. Gao, J. Wang, Y. Qin, Angew. Chem. Int. Ed. 55 (25) (2016) 7081–7085.

[28] J. Zhang, Z. Yu, Z. Gao, H. Ge, S. Zhao, C. Chen, S. Chen, X. Tong, M. Wang, Z. Zheng, Y. Qin, Angew. Chem. Int. Ed. 56 (3) (2017) 816–820.

[29] A.A. Dameron, D. Seghete, B.B. Burton, S.D. Davidson, A.S. Cavanagh, J.A. Bertrand, S.M. George, Chem. Mater. 20 (10) (2008) 3315–3326.

[30] X. Meng, J. Mater. Chem. A 5 (35) (2017) 18326–18378.

[31] M. Yu, H.H. Funke, R.D. Noble, J.L. Falconer, J. Am. Chem. Soc. 133 (6) (2011) 1748–1750.

[32] T.D. Gould, A. Izar, A.W. Weimer, J.L. Falconer, J.W. Medlin, ACS Catal. 4 (8) (2014) 2714–2717.

[33] S. Ishchuk, D.H. Taffa, O. Hazut, N. Kaynan, R. Yerushalmi, ACS Nano 6 (8) (2012) 7263–7269.

[34] Q. Peng, B. Gong, R.M. VanGundy, G.N. Parsons, Chem. Mater. 21 (5) (2009) 820–830.

[35] B. Yoon, D. Seghete, A.S. Cavanagh, S.M. George, Chem. Mater. 21 (22) (2009) 5365–5374.

[36] L. Machala, J. Tuček, R. Zbořil, Chem. Mater. 23 (14) (2011) 3255–3272.

[37] N.J. Tang, W. Zhong, C.T. Au, A. Gedanken, Y. Yang, Y.W. Du, Adv. Funct. Mater. 17 (9) (2007) 1542–1550.

[38] J. Tuček, R. Zbořil, A. Namai, S.-i. Ohkoshi, Chem. Mater. 22 (24) (2010) 6483–6505.